

Enhanced upward heat transport at deep submesoscale ocean fronts

Lia Siegelman^{1,2,3*}, Patrice Klein^{1,2,4}, Pascal Rivièr^e³, Andrew F. Thompson¹, Hector S. Torres², Mar Flexas¹ and Dimitris Menemenlis^{1,2}

The ocean is the largest solar energy collector on Earth. The amount of heat it can store is modulated by its complex circulation, which spans a broad range of spatial scales, from metres to thousands of kilometres. In the classical paradigm, fine oceanic scales, less than 20 km in size, are thought to drive a significant downward heat transport from the surface to the ocean interior, which increases oceanic heat uptake. Here we use a combination of satellite and in situ observations in the Antarctic Circumpolar Current to diagnose oceanic vertical heat transport. The results explicitly demonstrate how deep-reaching submesoscale fronts, with a size smaller than 20 km, are generated by mesoscale eddies of size 50–300 km. In contrast to the classical paradigm, these submesoscale fronts are shown to drive an anomalous upward heat transport from the ocean interior back to the surface that is larger than other contributions to vertical heat transport and of comparable magnitude to air-sea fluxes. This effect can remarkably alter the oceanic heat uptake and will be strongest in eddy-rich regions, such as the Antarctic Circumpolar Current, the Kuroshio Extension and the Gulf Stream, all of which are key players in the climate system.

Vertical heat transport (VHT) is one of the key mechanisms by which the ocean regulates Earth's climate. Munk and Wunsch¹ first postulated that VHT is balanced by an upward component due to the large-scale mean flow (>300 km) and a downward component explained by fine-scale diffusive processes (<20 km). However, recent studies^{2,3} highlighted the importance of mesoscale eddies (50–300 km) for VHT. Thus, global VHT by mean flow and diffusion are now thought to be both downward and balanced by an upward eddy heat flux, with the mean and eddy components generally being the largest contributors².

Mesoscale eddies are intensified in energetic areas such as the Antarctic Circumpolar Current (ACC), Kuroshio Extension and Gulf Stream⁴. They are known to drive the production of submesoscale fronts (<20 km), that is, regions that separate waters of different densities^{5–9}, which are ubiquitous on satellite images of ocean colour (Fig. 1). To date, submesoscale fronts were mainly thought to be confined to the ocean surface mixed layer (~100 m deep)^{8,9}. This is because, in the classical model, motions below the mixed-layer are broadly assumed to be in geostrophic balance (a balance between Coriolis and horizontal pressure forces), which prevents the formation of strong density gradients¹⁰. As a consequence, fine scales below the mixed-layer are still principally associated with diffusive processes that drive downward heat transport. However, a handful of studies suggest that submesoscale fronts associated with upward heat transport may also penetrate below the mixed layer^{11–14}. Yet, these studies do not explain the formation mechanism of these submesoscale fronts because they are confined to small domains (<50 km). Observational evidence over domains sufficiently large to capture multiple mesoscale eddies and their associated submesoscale fronts are needed for the closure of oceanic VHT. Such measurements are still lacking because capturing fine spatial and temporal scales over extended domains lie at the edge of our observational capabilities.

Here we meet this observational challenge by analysing a unique dataset collected by an instrumented elephant seal in the ACC. The seal data revealed the presence of numerous deep-reaching submesoscale fronts that extend well below the mixed-layer and are principally found on eddies' edges. We then developed a pioneering methodology that combines satellite and seal observations to retrieve a three-dimensional (3D) synoptic view of ocean dynamics from the meso- to submesoscale. The results explicitly demonstrate that deep-reaching submesoscale fronts are generated by the strain field associated with co-interacting mesoscale eddies. By invoking the properties of mesoscale turbulence, we explain why deep-reaching fronts, counterintuitively, drive an enhanced VHT below the surface mixed layer that is directed upward; this is also supported by a numerical model analysis (Supplementary Information). The associated VHT is larger than the mean flow and eddy contributions², and of similar magnitude to air-sea fluxes¹⁵. This effect is argued to crucially limit oceanic heat uptake and therefore to alter the ocean heat storage capacity.

Frontal region sampled by elephant seal and satellite

Measurements were collected by a southern elephant seal (*Mirounga leonina*) in the Kerguelen area (Indian sector of the Southern Ocean, Fig. 1) during the austral spring and summer. The dataset has a horizontal resolution of 1 km, a vertical resolution of 1 m and extends from the surface down to 400 m in the ocean interior. Over a period of more than three months and a distance that exceeded 5,000 km, the seal continuously recorded temperature, conductivity and pressure, from which the buoyancy b (opposite sign to density) was derived (Methods). An example of the buoyancy field is shown in Fig. 2a–c. In addition, satellite altimeter observations supply daily horizontal fields of sea surface height (SSH), a proxy of surface pressure, with an effective resolution sufficient to resolve mesoscale eddies of size of 50–100 km.

¹Environmental Science and Engineering, California Institute of Technology, Pasadena, CA, USA. ²Jet Propulsion Laboratory, California Institute of Technology, Pasadena, CA, USA. ³Université de Brest, CNRS, IRD, Ifremer, LEMAR, Plouzané, France. ⁴Université de Brest, CNRS, IRD, Ifremer, LOPS, Plouzané, France. *e-mail: lsiegelman@caltech.edu

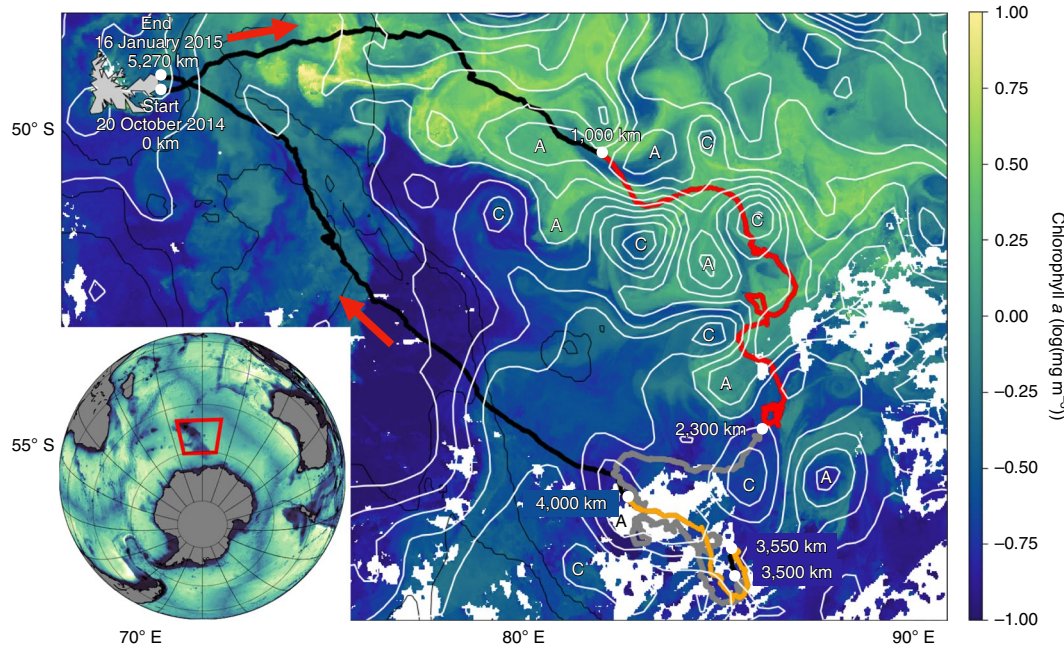


Fig. 1 | Study region (22 December 2014). A three-month seal trajectory (black line) superimposed with a snapshot of chlorophyll *a* and SSH (white contours). Three regions are highlighted: the highly turbulent area (red), the weakly turbulent area (grey) and the southern eddy edge (orange). Cyclones (C) and anticyclones (A) are identified from elliptic SSH contours. Hyperbolic SSH contours located inbetween eddies identify the strain field (Fig. 3a). Red arrows indicate the direction of the seal. Bathymetry contours of 0.5, 2 and 3 km (thin black lines) from NOAA ETOPO5 (National Oceanic and Atmospheric Administration's Earth topography five minute grid) outline the Kerguelen plateau. Inset: Kerguelen region (red polygon).

The area sampled by the seal from 1,000 to 2,300 km (red line in Fig. 1), that is, from 2 November to 24 November 2014, is rich in eddies and lies within the energetic ACC¹⁶, as illustrated by the SSH contours in Fig. 1. The seal crossed numerous co-interacting cyclonic (low SSH) and anticyclonic (high SSH) mesoscale eddies. Geostrophic currents, derived from the SSH, reach values of 1 m s^{-1} around the eddy edges (Fig. 2a) and are similar to those found in the Gulf Stream and the Kuroshio Extension, the two other most energetic ocean currents⁴. This area is thus representative of the flow field encountered within eddy-rich regions of the world oceans, and will receive particular emphasis in this study. The other areas crossed by the seal (Fig. 1) are much less energetic (Extended Data Fig. 1).

A comparison between the satellite SSH and buoyancy anomalies sampled by the seal in the turbulent area (Fig. 2a–c and Supplementary Fig. 1a–c) highlights the expected vertical structure of the mesoscale eddies¹⁰: buoyancy anomalies are positive and bowl shaped in anticyclonic eddies (high SSH) and negative and reversed bowl shaped in cyclonic eddies (low SSH, Fig. 2a–c and Extended Data Fig. 1a–c). The combination of satellite observations of SSH and seal measurements of buoyancy provides a synoptic 3D view of the flow field encountered by the seal, and, in particular, of the eddy field, which can extend down to depths of at least 400 m. Supplementary Information gives a more detailed analysis of the consistency at mesoscale between these two independent datasets.

Frontal structures, or buoyancy fronts, are identified by the along-track derivative of buoyancy and are defined as $b_s = \partial b / \partial s$, where s is the curvilinear abscissa, that is, the along-track direction. The fronts, shown in Fig. 2d, have a width between 5 and 20 km and are thus submesoscale features. Indeed, the Rossby radius of deformation in the Kerguelen area is $\sim 15 \text{ km}$ (ref. ¹⁷), which corresponds to an eddy radius of $\sim 50 \text{ km}$ (refs. ^{17,18}), consistent with the SSH observations (Fig. 2a). These fronts are well-resolved by the seal's 1 km horizontal resolution measurements. They are more numerous below the mixed layer and extend down to at least 400 m.

Large buoyancy gradients are preferentially found at the edges of the mesoscale eddies and in-between them. Buoyancy gradient magnitudes reach values larger than $5 \times 10^{-7} \text{ s}^{-2}$. The root mean squared (r.m.s.) of the lateral gradient of buoyancy, used as an indicator of the gradient magnitude, is larger than $0.5 \times 10^{-7} \text{ s}^{-2}$, regardless of depth (Extended Data Fig. 2a). Compared to the few other existing submesoscale-resolved datasets^{19–21}, these values are of the same order of magnitude, which highlights the important frontal activity of the area.

Frontal dynamics in the ocean interior

Figure 3 illustrates how the production of horizontal gradients of buoyancy is driven by a pure strain field, which corresponds to the hyperbolic regions in-between co-interacting eddies⁵, as can be seen in Fig. 1. In the schematic Fig. 3a, the strain field (black arrows) stretches a tracer patch in the y direction and compresses it in the x direction. This leads to the formation of strong horizontal gradients of buoyancy, or fronts, at submesoscale that are associated with a growth rate related to the strain rate $u_x = \frac{\partial u}{\partial x}$ (Fig. 3b).

To assess the relevance of this mechanism in the Kerguelen area, we analysed the background strain field in relation to the observed buoyancy gradients. We used daily finite size Lyapunov exponents (FSLEs)²² computed from satellite-derived geostrophic velocities to characterize the strain field properties (Methods). FSLEs indicate both the orientation and timescale (colour bar in Fig. 4a) of the stretching and compression induced by the strain field (respectively, the red and blue curves in Figs. 3a and 4a). As illustrated in Fig. 3a, we expect a tracer patch, or equivalently a buoyancy anomaly, to be aligned with stretching FSLE²². The spatial distribution of FSLE (Fig. 4a and Extended Data Fig. 3) confirms that regions in-between eddies and on eddy edges are prone to the formation of strong horizontal buoyancy gradients ($|b_x|$). However, the seal's trajectory is often oblique rather than perpendicular to the buoyancy fronts, which may lead to an underestimation of the front's magnitude. Therefore, to correct for the seal's orientation with respect

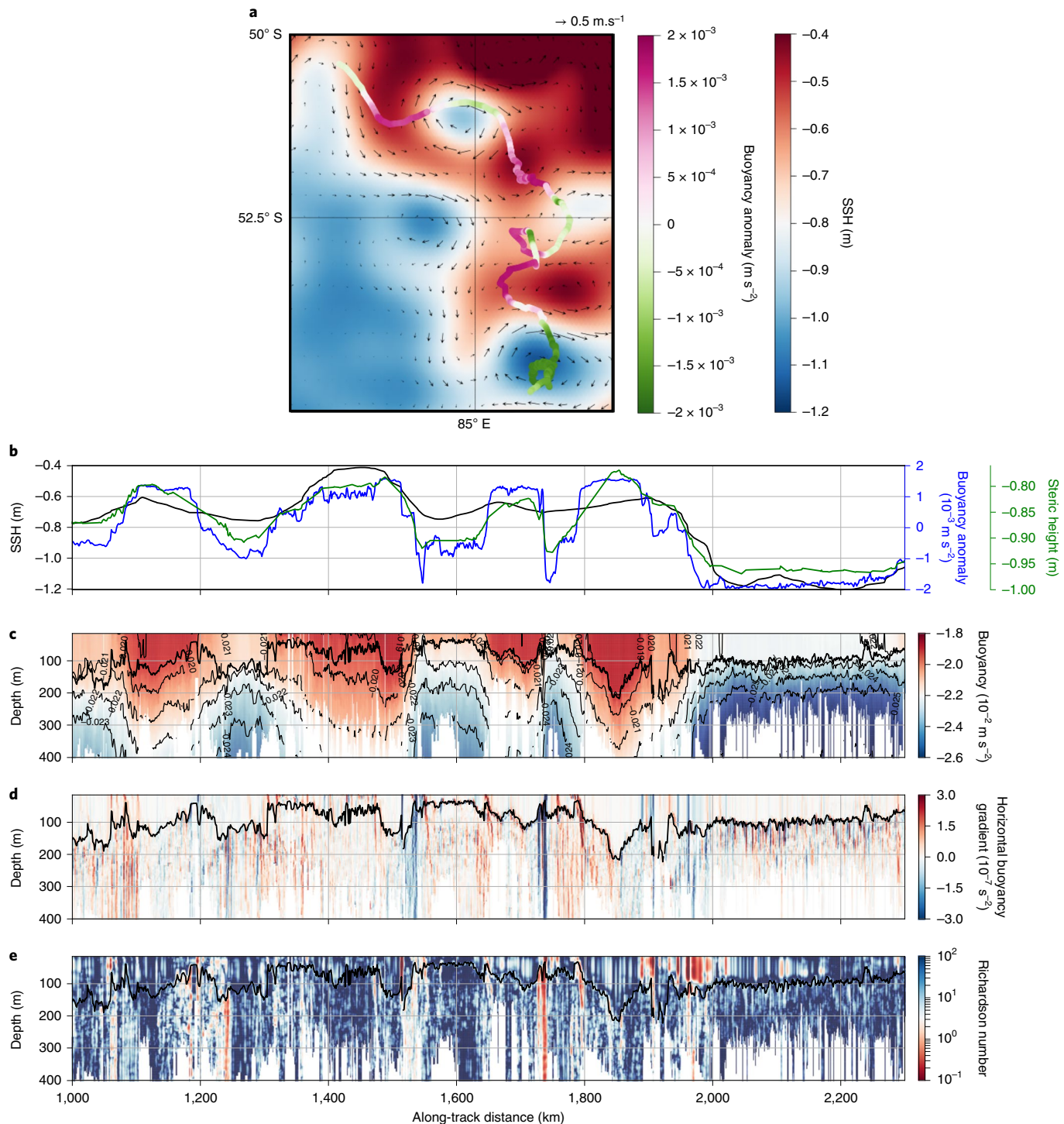


Fig. 2 | Characteristics of the strongly turbulent area (red in Fig. 1). a, A snapshot (13 December 2014) of SSH and geostrophic currents (black arrows) superimposed with the surface buoyancy anomaly measured by the seal from 2 November 2014 to 24 November 2014. **b,** An along-seal-track time series of SSH (black line), seal-measured buoyancy anomaly (blue line) and steric height (green line) (Supplementary Information). **c,** The seal's vertical section of buoyancy. The thin black lines are isopycnals. **d,** The seal's vertical section of lateral buoyancy gradients, b_s . **e,** The seal's vertical section of the Richardson number. The mixed layer depth (MLD) is shown by a thick black line in **c-e**.

to the FSLE it encounters, buoyancy gradients were first normalized by the angle between the seal's trajectory and the FSLE direction (Methods). Note that the normalized buoyancy gradients are now referred to as b_x , where the subscript x refers to the direction normal to the stretching FSLE (Fig. 3a). We then compared the along-track time series of stretching FSLE estimated along the seal's

path with the normalized buoyancy gradients at 300 m (a comparison with buoyancy gradients at different depths below the mixed layer produces similar results). There is good agreement between the FSLE and normalized buoyancy gradients at 300 m (Fig. 4 and Extended Data Fig. 4a), as well as a consistent relationship that links the two (Fig. 4b). The two time series are strongly intermit-

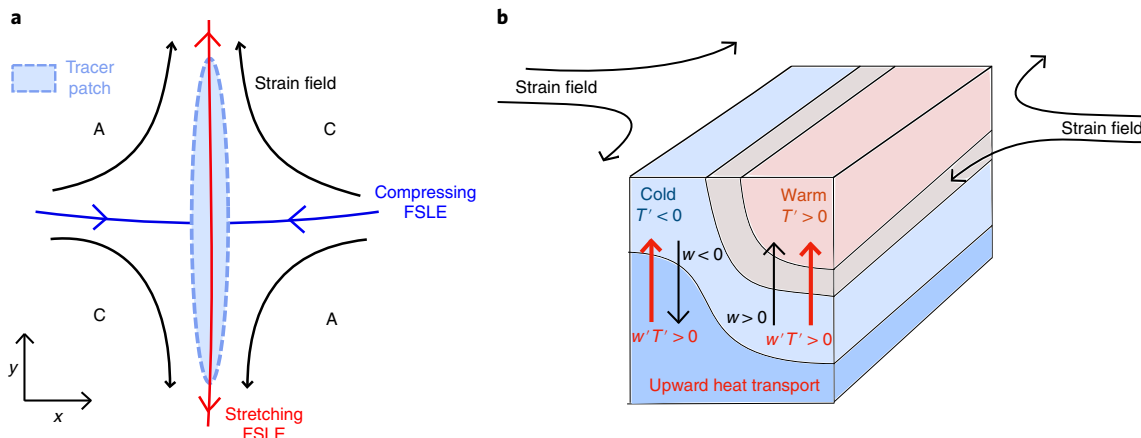


Fig. 3 | Strain field, frontogenesis and VHT. **a**, A horizontal slice (x,y) of a tracer patch (light blue) in a strain field (black arrows). The strain elongates (compresses) the tracer in the y (x) direction¹⁰. Red (blue) FSLE (proxy of strain) arrows identify horizontal stretching (compressing) directions. The fronts are aligned with the stretching FSLE. **b**, A 3D slice of the strain-induced submesoscale front. The thin black lines are isotherms. Vertical velocities (w , straight black arrows) develop in response to the front intensification. As the temperature and w anomalies are positively correlated, frontogenesis-induced VHT is upward (see Methods for a full description).

tent. Peaks of FSLE and buoyancy gradients are often co-located (Fig. 4a,b and Extended Data Fig. 4a). Note that similar results are obtained with non-normalized gradients, which demonstrates that no bias is added via the normalization. Combined together, these two datasets provide observational evidence of how an eddy strain field, diagnosed at the sea surface, drives strong buoyancy gradients at a submesoscale in the ocean interior.

A comparison between panels c and d in Fig. 2 further reveals that, whereas mesoscale buoyancy anomalies are slanted on the vertical, as evidenced by the bowl-shaped structures of buoyancy (panel c), buoyancy fronts at the submesoscale are almost vertical (panel d). This density slope property is related to the dynamical regime that drives these structures and can be quantified by the non-dimensional Richardson number Ri (Methods). The small Ri values observed in Fig. 2d suggest an energetic ageostrophic regime associated with intense vertical currents. The emergence of these vertical currents, w , counterbalances the formation of sharp submesoscale fronts generated by the ambient strain field. This mechanism is referred to as frontogenesis²³ and is sketched in Fig. 3b. It leads to an equilibrium that is captured by the classical omega equation, which involves the vertical current field w , the strain field u_x and the lateral gradient of buoyancy field b_x . Here we diagnose the vertical currents w by solving the 2D (x,z) quasi-geostrophic (QG) version of the omega equation²³ (Methods), with b_x obtained from seal observations and u_x estimated from stretching FSLE (Fig. 4). However, compared to the full omega equation, there is a tendency for the vertical currents diagnosed here to be underestimated by ~ 1.4 (Methods).

The vertical section of w shown in Fig. 5b reveals positive and negative w values with large magnitudes of up to 100 m d^{-1} , that is, almost an order of magnitude greater than that attributed to mesoscale eddies alone²⁴. Vertical currents have a width of 5–10 km. They are intensified in the ocean interior, below the mixed layer down to at least 400 m, and do not necessarily penetrate into the mixed layer. The continuous vertical extent of these vertical currents highlights the crucial role played by deep-reaching submesoscale fronts in connecting the ocean interior to the surface. The w field is characterized by the same intermittency present in the FSLE and buoyancy gradient fields (Figs. 2d, 4c, 5b and Extended Data Fig. 4b). Large w magnitudes are co-located with strong buoyancy gradients and intense FSLE, and are therefore mostly found on the edges of, and in-between, eddies.

The analysis of the vertical currents presented here is supported by a comparison with a realistic regional numerical model with a 1.5 km horizontal resolution (Supplementary Information gives more details on the model). The values of w derived from the observations are comparable to, although smaller than, those obtained in the model (Extended Data Fig. 5a). Overall, these results suggest that the vertical pathway provided by deep ocean fronts in the spring and summer is likely a generic mechanism throughout the ocean. This deep-reaching vertical pathway has important consequences for the vertical transfer of heat between the ocean interior and the surface mixed layer, as explored in the next section.

VHT at deep submesoscale fronts

Oceanic heat transport was estimated from temperature and vertical velocity anomalies, from the surface down to 400 m depth (Fig. 5a,b). A vertical section of this transport (Methods gives the calculation) is shown in Fig. 5c, in which a positive (negative) value indicates an upward (downward) heat transport. Positive values result from frontogenesis processes, that is, the production of fronts, as illustrated in Fig. 3b. Negative values arise from frontolysis processes, that is, the destruction of fronts (Supplementary Information). Heat transport is strongly enhanced at the location of submesoscale fronts generated by the background strain field and has a local amplitude that reaches $2,000 \text{ W m}^{-2}$ below the surface mixed layer, and extends down to at least 400 m, consistent with the high-resolution regional model (Extended Data Figs. 5b and 6) and, surprisingly, of the same order of magnitude as instantaneous air-sea heat fluxes¹⁹.

We explored the contribution of fine oceanic scales to the domain-averaged VHT. Averaged VHT within the eddy-rich area of the ACC sampled by the seal (1,000–2,000 km, in red in Fig. 1) is directed upward, that is, from the ocean interior back to the surface (Fig. 5f). This direction is strikingly opposite to that induced by the diffusive processes used in the classical paradigm. However, this result can be understood in terms of the direct cascade of potential energy, a well-known property of mesoscale eddy turbulence²⁵. The direct cascade implies that frontogenesis statistically dominates frontolysis, and thus that the net VHT associated with submesoscale fronts is positive (Supplementary Information), which is also striking in the model outputs (Extended Data Fig. 6). Furthermore, the heat transport magnitude reached an averaged value of $\sim 100 \text{ W m}^{-2}$ at 200 m (Fig. 5f). Remarkably, this value is an order of magnitude larger than

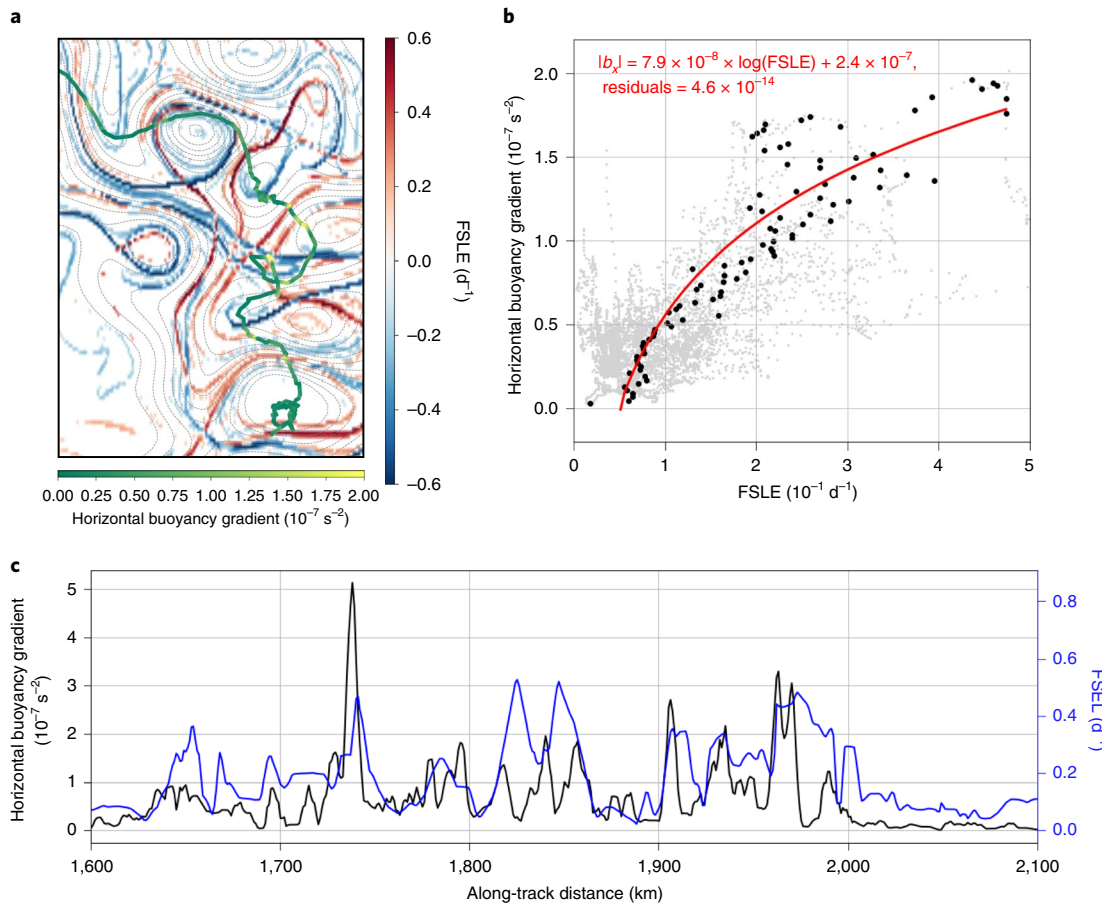


Fig. 4 | FSLE and horizontal buoyancy gradients ($|b_x|$). a, A snapshot of FSLE and SSH contours (dashed grey) for 13 November 2014 in the strongly turbulent region (red line in Fig. 1), with surface $|b_x|$ from 2 November to 24 November 2014. **b,** A scatter plot of along-seal-track stretching FSLE and $|b_x|$ at 300 m, over the entire trajectory, after a 30 km moving average and averaging the y axis over 100 bins (black dots), with unaveraged data in grey. The relationship obtained between FSLE and $|b_x|$ is given in red. **c,** Along-seal-track time series of stretching FSLE (blue) and $|b_x|$ at 30 m (black) after a 5 km moving average.

that associated with mesoscale eddies alone²⁶, which is, along with the mean flow, traditionally thought to be the main contributor to VHT². It is also of comparable magnitude to domain-averaged air-sea heat fluxes¹⁵, which illustrates a potential coherent pathway that links the ocean interior to the atmosphere. Note that the percentage of seal dives decreases with depth (grey line in Fig. 5f), from 100 to 40% between 200 and 400 m. This probably accounts for a part of the r.m.s. decrease (stagnation) of temperature (velocity) anomalies below 200 m, as one would have expected⁵ (Fig. 5d,e). As a consequence, the already unexpected strong heat transport (Fig. 5c,f) is likely to be underestimated because of it, in addition to the conservative estimate of the vertical currents discussed in the previous section. Indeed, the domain-integrated heat transport from the high-resolution numerical simulation yields a similar—although stronger—positive VHT (Extended Data Fig. 7) with, for instance, a value of $\sim 140 \text{ W m}^{-2}$ at 200 m. As such, these results strongly contrast with the classical paradigm based on diffusive heat transport, as they emphasize the existence of an intense and upward heat transport in the ocean interior well below the ocean surface mixed layer that is preferentially localized in strain-dominated areas (Extended Data Fig. 6).

The data presented here provide the first observational evidence of a large and anomalous, that is, upward, heat transport associated with deep-reaching submesoscale fronts in an eddy-rich area of the world ocean. The observations, supported by a high-resolution regional model (Supplementary Information), highlight the crucial

role played by submesoscale frontal dynamics in the ocean interior, well below the ocean surface mixed layer, for oceanic heat transport.

In summary, the deep-reaching frontal dynamics and its associated large positive VHT, observed here in numerous sharp fronts of the ACC, are driven by mesoscale eddies and are likely to occur widely in the ocean, such as in the eddy-rich Gulf Stream and Kuroshio Extension, all of which are key players in the climate system. It potentially plays an important role by, for instance, exacerbating restratification processes as warm (cold) waters become warmer (colder). Furthermore, a first-order estimation indicates that these deep ocean fronts lead to an additional increase of the sea surface temperature that ranges between ~ 0.2 and $\sim 0.6^\circ\text{C}$ within a month (Methods gives the calculation and caveats), which illustrates the potential impact of deep-reaching ocean fronts on air-sea fluxes and how they can substantially limit oceanic heat uptake from the atmosphere.

These observational results suggest revisiting current estimates of the Earth's heat budget and stress the need to account for small-scale physics, not only within, but also below, the ocean surface mixed layer, in the prediction of future climate states. Inaccurate representation of such physics could considerably underestimate the amount of heat transferred from the ocean interior back to the surface and, as a consequence, potentially overestimate the amount of heat the ocean can absorb. Finally, these results may have a far greater scope as the evidence for intense vertical currents associated

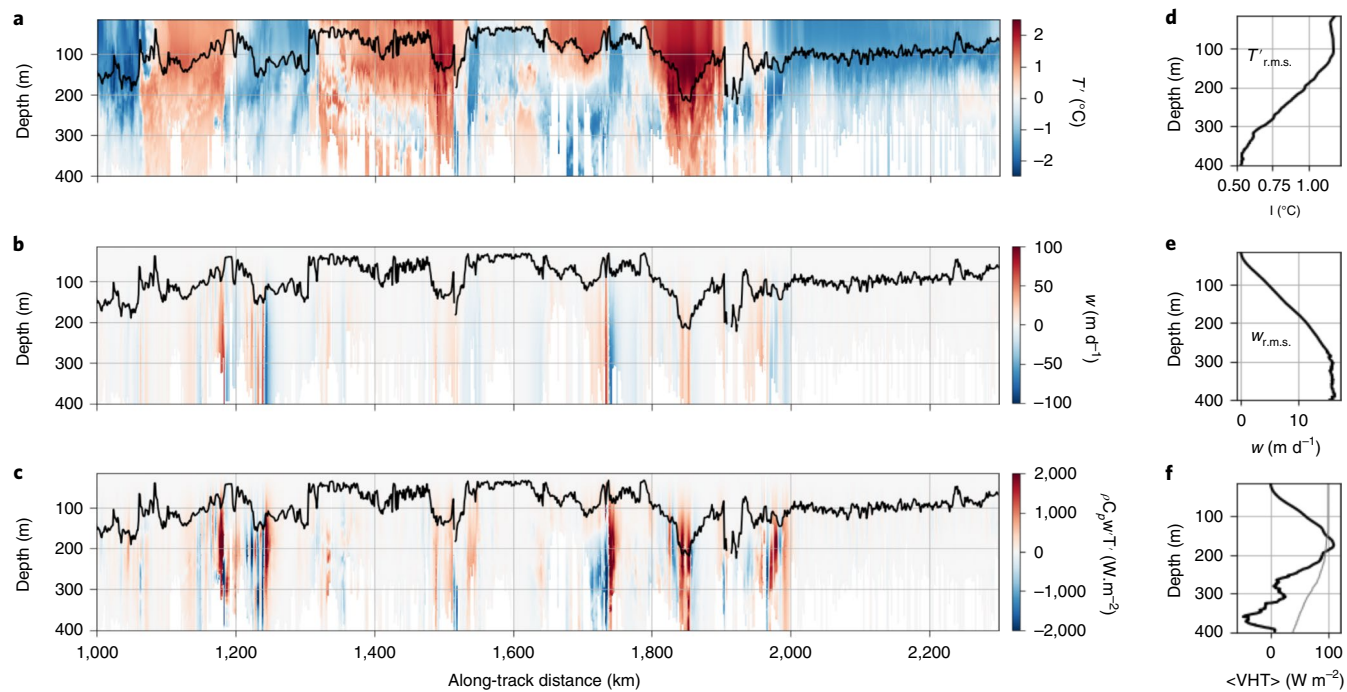


Fig. 5 | Temperature anomaly, vertical velocity and VHT. **a–c**, The vertical section of the seal-sampled temperature anomaly (T) (**a**), vertical velocity derived from the seal and satellite data with equation (3) (**b**) and VHT (**c**), as defined in Methods. In **a–c**, the MLD is in bold black. **d,e**, The r.m.s. (z) from 1,000 to 2,000 km of the temperature anomaly (**d**) and the vertical velocity (**e**). **f**, Averaged VHT ($\langle VHT \rangle$) (black line). $\langle VHT \rangle$ reaches $\sim +110 \text{ W m}^{-2}$ at 200 m. The percentage of profiles (grey line) goes from 100% at 20 m to 40% at 400 m.

with the deep-reaching ocean fronts presented here also indicates an efficient pathway for the transport of chemical and biological tracers, with potential major implications for biogeochemical systems.

Online content

Any methods, additional references, Nature Research reporting summaries, source data, extended data, supplementary information, acknowledgements, peer review information; details of author contributions and competing interests; and statements of data and code availability are available at <https://doi.org/10.1038/s41561-019-0489-1>.

Received: 18 June 2019; Accepted: 16 October 2019;

Published online: 02 December 2019

References

- Munk, W. & Wunsch, C. Abyssal recipes II: energetics of tidal and wind mixing. *Deep Sea Res. Part I* **45**, 1977–2010 (1998).
- Wolfe, C., Cessi, P., McClean, J. & Maltrud, M. Vertical heat transport in eddying ocean models. *Geophys. Res. Lett.* **35**, L23605 (2008).
- Griffies, S. M. et al. Impacts on ocean heat from transient mesoscale eddies in a hierarchy of climate models. *J. Clim.* **28**, 952–977 (2015).
- Ferrari, R. & Wunsch, C. Ocean circulation kinetic energy: reservoirs, sources, and sinks. *Annu. Rev. Fluid Mech.* **41**, 253–282 (2009).
- Klein, P. & Lapeyre, G. The oceanic vertical pump induced by mesoscale and submesoscale turbulence. *Annu. Rev. Mar. Sci.* **1**, 351–375 (2009).
- Ferrari, R. A frontal challenge for climate models. *Science* **332**, 316–317 (2011).
- Mahadevan, A. The impact of submesoscale physics on primary productivity of plankton. *Annu. Review Mar. Sci.* **8**, 161–184 (2016).
- McWilliams, J. C. Submesoscale currents in the ocean. *Proc. R. Soc. A* **472**, 20160117 (2016).
- Lévy, M., Frank, P. J. & Smith, S. K. The role of submesoscale currents in structuring marine ecosystems. *Nat. Commun.* **9**, 4758 (2018).
- Vallis, G. K. *Atmospheric and Oceanic Fluid Dynamics* (Cambridge Univ. Press, 2017).
- Taylor, J. R. & Ferrari, R. Ocean fronts trigger high latitude phytoplankton blooms. *Geophys. Res. Lett.* **38**, 23 (2011).
- Thomas, L. N., Taylor, J. R., Ferrari, R. & Joyce, T. M. Symmetric instability in the Gulf Stream. *Deep. Sea Res. Pt II* **91**, 96–110 (2013).
- Bachman, S. D. & Taylor, J. R. Modelling of partially-resolved oceanic symmetric instability. *Ocean Model.* **82**, 15–27 (2014).
- Yu, X. et al. An annual cycle of submesoscale vertical flow and restratification in the upper ocean. *J. Phys. Oceanogr.* **49**, 1439–1461 (2019).
- Large, W. G. & Yeager, S. The global climatology of an interannually varying air-sea flux data set. *Clim. Dynam.* **33**, 341–364 (2009).
- Hogg, A. M. et al. Recent trends in the Southern Ocean eddy field. *J. Geophys. Res. Ocean* **120**, 257–267 (2015).
- Chelton, D. B., DeSzoeke, R. A., Schlax, M. G., El Naggar, K. & Siwertz, N. Geographical variability of the first baroclinic Rossby radius of deformation. *J. Phys. Oceanogr.* **28**, 433–460 (1998).
- Chelton, D. B., Schlax, M. G., Freilich, M. H. & Milliff, R. F. Satellite measurements reveal persistent small-scale features in ocean winds. *Science* **303**, 978–983 (2004).
- Thompson, A. F. et al. Open-ocean submesoscale motions: a full seasonal cycle of mixed layer instabilities from gliders. *J. Phys. Oceanogr.* **46**, 1285–1307 (2016).
- duPlessis, M., Swart, S., Ansorge, I. J. & Mahadevan, A. Submesoscale processes promote seasonal restratification in the Subantarctic Ocean. *J. Geophys. Res. Ocean* **122**, 2960–2975 (2017).
- Viglione, G. A., Thompson, A. F., Flexas, M. M., Sprintall, J. & Swart, S. Abrupt transitions in submesoscale structure in southern Drake Passage: glider observations and model results. *J. Phys. Oceanogr.* **48**, 2011–2027 (2018).
- d’Ovidio, F. & Fernández, V. & Hernández-García, E. & López. Mixing structures in the Mediterranean Sea from finite-size Lyapunov exponents. *Geophys. Res. Lett.* **31**, L17203 (2004).
- Hoskins, B. J., Draghici, I. & Davies, H. C. A new look at the ω -equation. *Q. J. R. Meteorol. Soc.* **104**, 31–38 (1978).
- McGillivray Jr, D. J. Mechanisms of physical–biological–biogeochemical interaction at the oceanic mesoscale. *Annu. Review Mar. Sci.* **8**, 125–159 (2016).
- Salmon, R. Baroclinic instability and geostrophic turbulence. *Geophys. Astrophys. Fluid Dyn.* **15**, 167–211 (1980).
- Su, Z., Wang, J., Klein, P., Thompson, A. F. & Menemenlis, D. Ocean submesoscales as a key component of the global heat budget. *Nat. Commun.* **9**, 775 (2018).

Publisher’s note Springer Nature remains neutral with regard to jurisdictional claims in published maps and institutional affiliations.

This is a U.S. government work and not under copyright protection in the U.S.; foreign copyright protection may apply 2019

Methods

SSH and geostrophic currents. The SSH used to retrieve the mesoscale dynamics of the Kerguelen area ($67^{\circ}\text{--}91^{\circ}\text{E}$, $48^{\circ}\text{--}58^{\circ}\text{S}$) is composed of the mean dynamic topography CNES/CLS 2015²⁷ and the sea level anomaly maps produced by the DUACS (data unification and altimeter combination system) processing chain that merges the multi-altimeter along-track data. This specific regional dataset was produced in the context of the DUACS-HR project, which aimed to increase the resolution of altimetry maps by applying recently developed methods, such as dynamic interpolation²⁸. The period from October 2014 to January 2015 benefits from an extremely favourable satellite coverage of four altimeters (AltiKa, Jason-2, Cryosat-2 and HY-2), which allowed a very good spatial and temporal sampling. The temporal resolution is daily and, as estimated in Ballarotta et al.²⁹, the spatial effective resolution of the gridded anomalies approaches 40 km in wavelength. Using the geostrophic approximation, geostrophic surface currents (u, v) are derived from SSH following¹⁰:

$$u = -\frac{g}{f} \frac{\partial \text{SSH}}{\partial y}, \quad v = \frac{g}{f} \frac{\partial \text{SSH}}{\partial x} \quad (1)$$

where g is gravity and f the Coriolis parameter.

FSLE. Instead of using a direct estimate of the strain rate (that is, du/dx calculated directly from SSH, Fig. 3) that only describes the buoyancy gradient's growth rate, we use FSLEs. Indeed, FSLEs have the advantage of exploiting both the spatial and temporal variability of the velocity field deduced from SSH, and consequently provide information about both the growth rate and orientation of elongated buoyancy gradients^{30,31}. FSLE is a Lagrangian diagnostic that measures the separation of close initial particles embedded in given flow field. The separation's growth rate is defined as:

$$\lambda(d_0, d_f) = \frac{1}{\tau} \log\left(\frac{d_f}{d_0}\right) \quad (2)$$

where d_0 and d_f are the initial and final separation distances, respectively, and τ the first time at which a separation d_f is reached. FSLE has the dimension of time⁻¹. FSLE is particularly suited to diagnose the properties of a strain field. Positive (negative) FSLE indicate that patches of particles are being stretched (compressed) in a given direction determined by the background strain field. As such, large positive (negative) FSLE values indicate regions of strong stretching (compression) (Fig. 3a and Supplementary Information give more details). Here, positive (negative) FSLE are computed backward (forward) in time²².

For the Kerguelen area, 88 daily maps of altimetry-based FSLEs were computed following d'Ovidio et al.²² and using the geostrophic velocities derived from the SSH. The parameters were chosen close to those of d'Ovidio et al.²² with $d_0=0.04^{\circ}$ and $d_i=1^{\circ}$, that is, a final separation distances of about 110 km.

An along-track time series of stretching (that is, positive) FSLE was extracted along the seal's path to capture the stretching direction and intensity of the strain field. A subsequent 5 km window moving average was applied to remove the strong intermittency present in the raw data (Fig. 4 and Extended Data Fig. 4a). Stretching FSLEs were then compared to lateral gradients of buoyancy sampled by the seal.

Southern elephant seal measurements. A newly released in situ dataset collected in the austral summer by a female southern elephant seal during her three-month post-breeding trip (20 October 2014 to 16 January 2015) east of the Kerguelen Islands (Indian sector of the Southern Ocean, Fig. 1) was analysed. Compared to previous tags mounted on elephant seals, this one recorded every single dive realized by the animal (>80 dives per day) at high-resolution as opposed to 2–5 dives per day for previous tags. The seal was localized through the Argos satellite system and was equipped with sensors that recorded conductivity, temperature and pressure (CTD-Satellite Relay Data Logger) at a continuous frequency of 0.5 Hz. Only the ascending phase of a dive was used because it is more uniform in speed and direction compared to the descent when the seal dives sinuously to forage³². The dataset comprised 6,333 dives, which corresponds to a cumulative length of 5,270 km with a median spacing between two dives of 700 m (Extended Data Fig. 8a). Dives, which could be as deep as 500–1,000 m, lasted less than 25 min and were separated by intervals of a few minutes during which the seal breathes but does not transit. More than 80% of the dives reached a depth of at least 200 m, 50% reached 300 m and 35% reached 400 m or deeper.

To ensure a better accuracy of the temperature- and conductivity-derived salinity data, two additional steps were applied: first, a thermal cell effect correction was applied to the temperature and conductivity fields. A density inversion removal algorithm, which seeks the minimum adjustment of the salinity profile to achieve neutral stability, was subsequently applied to the salinity field. The accuracy of the final postprocessed data was $\pm 0.02^{\circ}\text{C}$ for the temperature and $\pm 0.03 \text{ g kg}^{-1}$ for salinity. More details on the postprocessing method and final data accuracy are given in Siegelman et al.³². Potential density was calculated from the corrected conservative temperature and absolute salinity with the TEOS-10 equation³³.

The animal in this study was handled in accordance with the Institut polaire français Paul-Emile Victor (IPEV) ethical and Polar Environment Committees

guidelines as part of the SNO-MEMO and IPEV program 109 (principle investigator H. Weimerskirch). The experimental protocols were approved by the Ethics Committee of IPEV and the Polar Environment Committees.

Buoyancy. Along-track time series of buoyancy, $b = g(1 - \rho/\rho_0)$, where g is gravity, ρ is potential density and $\rho_0=1,025 \text{ kg m}^{-3}$ is a reference density, revealed a variability that covers both the meso- and submesoscales. For the analysis, in particular the calculation of lateral buoyancy gradients $b_s = \partial b/\partial s$, buoyancy was first linearly interpolated along the seal's path onto a regular grid of 100 m resolution, which corresponds to the shortest along-track distance between two dives (Extended Data Fig. 8a). A moving average with a 1 km window was then applied such that the final dataset had a horizontal resolution of 1 km and a vertical resolution of 1 m. Buoyancy anomalies were resolved by multiple vertical profiles, such that the structures were not related to aliasing of the along-track data. The surface buoyancy anomalies in Fig. 2a,b were defined by the time series of the mean buoyancy from 15 to 50 m minus its mean value calculated from 15 to 50 m along the entire trajectory.

MLD. The MLD was defined as the level of a 0.03 kg m^{-3} density increase from 15 m depth.

Normalization of buoyancy gradients. As the seal's trajectory was more often oblique to the stretching FSLEs (it crossed rather than ran perpendicular to them (Extended Data Fig. 8b)) and buoyancy fronts were assumed to be aligned with the stretching FSLE, buoyancy gradients sampled by the seal needed to be corrected to account for the seal's orientation with respect to the FSLE it encountered. To do so, the buoyancy gradients were divided by the sine of the angle θ between the seal's trajectory and the FSLE direction. More precisely, θ is the angle between the FSLE eigenvector and the seal's path. To focus on the regions prone to the formation of submesoscales, only b_s associated with large FSLE ($>0.15 \text{ d}^{-1}$) were normalized and are referred to as b_x . However, a sensitivity analysis (which ranged from 0.1 to 0.3 d^{-1} , not shown here) to this threshold value led to similar results.

Link between strain, frontogenesis and VHT. The ambient strain field in Fig. 3a acts to elongate the tracer patch in the stretching direction (y direction) and to compress it in the x direction because the area of the tracer patch is conserved to the leading order¹⁰. This increases the tracer gradient in the x direction. The orientation and timescale of the strain field can be captured by FSLE. In Fig. 3a, the red (blue) FSLE lines identify the horizontal stretching (compressing) direction. This mechanism is particularly relevant for the formation of submesoscale fronts, which are thus aligned with the stretching FSLE (red line). Figure 3b shows a schematic illustration of the frontogenesis process. It corresponds to a 3D slice through a submesoscale front generated by a background mesoscale strain field (curved black arrows), like that in Fig. 3a. Warmer (or equivalently lighter) fluid (light red) is on the right of the Fig. 3b and colder (or equivalently heavier) fluid (light blue) is on the left. As a consequence, the VHT associated with frontogenesis is directed upward because of the positive correlation between the temperature and vertical velocity anomalies.

Richardson number. The non-dimensional Richardson number Ri , estimated from the seal measurements, is defined as $Ri \equiv f^2 N^2 / b_x^2$, with $N^2 = \partial b / \partial z$ the Brunt–Väissälä frequency and $b_x = \partial b / \partial x$ the normalized along-track lateral gradient of buoyancy. Ri characterizes the dynamic regime and can be interpreted as the steepness of the isopycnal slopes relatively to N/f , as $Ri = \frac{f^2}{N^2} \left(\frac{\partial b}{\partial z} \right)^2 = \frac{f^2}{N^2} \left(\frac{\partial x}{\partial z} \right)^2$. Thus, for $Ri > 1$, which corresponds to the QG regime^{34,35}, the steepness of the isopycnal slope, $\frac{\partial b}{\partial z}$, is small. For Ri close to one (that is, $Ri \leq 4$), which corresponds to the ageostrophic regime^{34,35}, the steepness of the isopycnal slope, $\frac{\partial b}{\partial z}$, is large. Seal observations suggest a strong ageostrophic regime, as instances of strong b_x , $|b_x| \geq 2.5 \times 10^{-7} \text{ s}^{-2}$, coincide with $Ri < 2$ (Fig. 2 and Extended Data Fig. 2b). Small Ri values ($Ri < 2$) indicate an ageostrophic regime in which the vertical currents are large^{34,35}.

Vertical velocities. Classical methods to diagnose vertical velocities are based on the Q-vector version of the omega equation^{23,36}. In this study, we used the QG version of the omega equation (Supplementary Information discusses this choice). Buoyancy fronts are assumed to be elongated along a stretching direction (red FSLE in Fig. 3a) such that the along-front gradient of buoyancy in the y direction is negligible with respect to the cross-front one (x direction). Thus, we considered the 2D version (x, z) of the QG omega equation. This equation assumes that the trajectory is normal to the front, that is, that the front is embedded in a pure strain field, which is achieved through the buoyancy gradient normalization mentioned above. This equation is:

$$N^2 w_{xx} + f^2 w_{zz} = -2 (u_x b_x)_x \quad (3)$$

where the subscripts indicate the derivatives. u_x is estimated from stretching FSLE derived from satellite altimetry and b_x , N^2 and f^2 are from the seal's measurements.

Equation (3) is solved using the flexible framework for spectrally solving differential equations provided by Dedalus³⁷.

Note that when the Richardson number is close to one, equation (3) underestimates the vertical velocities. When $Ri \approx 2$, the magnitude of this underestimation is of ~ 0.7 , which implies that the vertical velocities w' diagnosed at sharp fronts should be closer to $1.4w'$ (Supplementary Information gives more details).

Note also that this study focuses on strain-dominated regions. However, in other regions, for instance, within mesoscale eddies, the strain rate is weaker and its impact on the formation of horizontal gradients is counterbalanced by the impact of the relative vorticity, which leads to the formation of weaker gradients of buoyancy. In such regions, even though the 2D version of the omega equation is no longer appropriate and a 3D version needs to be used, the resulting vertical velocities are 7.5 times weaker than those associated to submesoscale fronts in strain-dominated regions⁵, like the ones considered in the present study.

VHT. The VHT is defined as $\rho C_p w' T'$, where $C_p = 3,985 \text{ J kg}^{-1} \text{ K}^{-1}$ is the specific heat capacity of seawater, $\rho = 1,025 \text{ kg m}^{-3}$ is the density of the fluid, and w' and T' are the vertical velocity and temperature anomalies, respectively.

Impact of deep-reaching ocean fronts on the mixed-layer temperature. The impact of the deep-reaching ocean fronts on the mixed-layer temperature, and therefore the sea surface temperature, is derived from a thermodynamic equation that captures the evolution of the mixed-layer temperature T . This approach has already been used and validated at leading order³⁶. The equation, integrated over the mixed-layer depth, is:

$$C \frac{dT}{dt} = S - \lambda T \quad (4)$$

where $C = \rho C_p H$ is the total heat capacity of the mixed layer, H is the mixed-layer depth, S is the heat transport at the base of the mixed layer due to deep-reaching fronts and $-\lambda T$ is the negative feedback from the air-sea heat fluxes. From equation (4), a positive S causes a higher temperature T , and hence a larger upward air-sea heat exchange λT .

A sensitivity analysis was carried out to assess the range of the mean mixed-layer temperature change due to submesoscales over a period of one month, which corresponds to the time spent by the seal in the turbulent region and the time span of the high-resolution model. We set S to vary between 50 and 100 W m⁻², as obtained from both the observational (Fig. 5f) and model (Extended Data Fig. 7) results, λ to vary between 15 and 2 W m⁻² K⁻¹, according to Vallis³⁸ and the mixed-layer H to vary between 100 and 200 m, which implies that C varies between $\sim 4 \times 10^8$ and $\sim 8 \times 10^8 \text{ J m}^{-2} \text{ K}^{-1}$. As a consequence, equation (4) integrated over one month indicates that the mean mixed-layer temperature increase ranges between ~ 0.2 and $\sim 0.6^\circ\text{C}$.

Note this is a first-order estimation that includes several caveats. In particular, this estimation does not take into account any subsequent atmospheric feedback on the ocean that may arise in response to these surface heat fluxes (λT). For instance, such a feedback may include interactions between the wind stress and SST anomalies at submesoscales³⁹, which may limit the mean temperature increase.

Data availability

The marine mammal data were collected and made freely available by the International MEOP Consortium and the national programs that contribute to it, and is available at www.meop.net/database/meop-databases/meop-sms-database-submesosc.html. The Ssalto/Duacs altimeter products were produced and distributed by the Copernicus Marine and Environment Monitoring Service with support from CNES, and is available at <http://marine.copernicus.eu/services-portfolio/access-to-products/>.

References

27. Rio, M. H. et al. Improving the altimeter-derived surface currents using high-resolution sea surface temperature data: a feasibility study based on model outputs. *J. Atmos. Ocean. Technol.* **33**, 2769–2784 (2016).
28. Ubelmann, C., Klein, P. & Fu, L. L. Dynamic interpolation of sea surface height and potential applications for future high-resolution altimetry mapping. *J. Atmos. Ocean. Technol.* **32**, 177–184 (2015).
29. Ballarotta, M. et al. On the resolutions of ocean altimetry maps. *Ocean Sci.* **15**, 1091–1109 (2019).
30. Waugh, D. W., Abraham, E. R. & Bowen, M. M. Spatial variations of stirring in the surface ocean: a case study of the Tasman Sea. *J. Phys. Oceanogr.* **36**, 526–542 (2006).
31. d'Ovidio, F., Isern-Fontanet, J., López, C., Hernández-García, E. & García-Ladona, E. Comparison between Eulerian diagnostics and finite-size Lyapunov exponents computed from altimetry in the Algerian Basin. *Deep. Sea Res. Pt I* **56**, 15–31 (2009).
32. Siegelman, L. et al. Correction and accuracy of high-and low-resolution CTD data from animal-borne instruments. *J. Atmospheric Ocean. Technol.* **36**, 745–760 (2019).
33. Intergovernmental Oceanographic Commission *The International Thermodynamic Equation of Seawater—2010: Calculation and Use of Thermodynamic Properties (Includes Corrections up to 31st October 2015)* (UNESCO, 2015); https://www.oceanbestpractices.net/bitstream/handle/11329/286/TEOS-10_Manual.pdf?sequence=1
34. Molemaker, J., McWilliams, J. & Yavneh, I. Baroclinic instability and loss of balance. *J. Phys. Oceanogr.* **35**, 1505–1517 (2005).
35. Thomas, L. N., Tandon, A. & Mahadevan, A. in *Ocean Modeling an Eddying Regime* (eds Hecht, M. W. & Hasumi, H.) 17–38 (Geophysical Monograph Series Vol. 177, American Geophysical Union, 2008).
36. Giordani, H., Prieur, L. & Caniaux, G. Advanced insights into sources of vertical velocity in the ocean. *Ocean. Dyn.* **56**, 513–524 (2006).
37. Burns, K. J., Vasil, G. M., Oishi, J. S., Lecoanet, D. & Brown, B. Dedalus: Flexible Framework for Spectrally Solving Differential Equations (Astrophysics Source Code Library, 2016).
38. Vallis, G. K. *Climate and the Oceans* (Princeton Univ. Press, 2012).
39. Foussard, A., Lapeyre, G. & Plougonven, R. Response of surface wind divergence to mesoscale SST anomalies under different wind conditions. *J. Atmos. Sci.* **76**, 2065–2082 (2019).

Acknowledgements

We thank K. Richards for his insightful comments, F. d'Ovidio for providing the code to compute FSLE. The elephant seal work was supported as part of the SNO-MEMO and by the CNES-TOSCA project Elephant seals as Oceanographic Samplers of submesoscale features led by C. Guinet with support of the French Polar Institute (programmes 109 and 1201). This research was carried out, in part, at the Jet Propulsion Laboratory, California Institute of Technology, under a contract with the National Aeronautics and Space Administration (NASA). High-end computing resources for the numerical simulation were provided by the NASA Advanced Supercomputing Division at the Ames Research Center. This work was partly funded by the CNES (OSTST-OSIW) and the Laboratoire d'Excellence LabexMER (ANR-10-LABX-19). L.S. is a NASA-JVSRP affiliate and is supported by a joint CNES-Région Bretagne doctoral grant. P.K. is supported by the NASA-CNES SWOT mission and a NASA Senior NPP Fellowship. A.F.T. is supported by the David and Lucille Packard Foundation and NASA grant NNX16AG42G. M.F. is supported by NASA grant NNX15AG42G.

Author contributions

L.S. and P.K. conceived the experiments, analysed the results and wrote the manuscript. D.M. and H.S.T. ran the numerical simulations. H.S.T. helped with analysing the regional simulation. L.S., P.K., P.R., A.F.T., H.S.T. and M.F. reviewed the manuscript.

Competing interests

The authors declare no competing interests.

Additional information

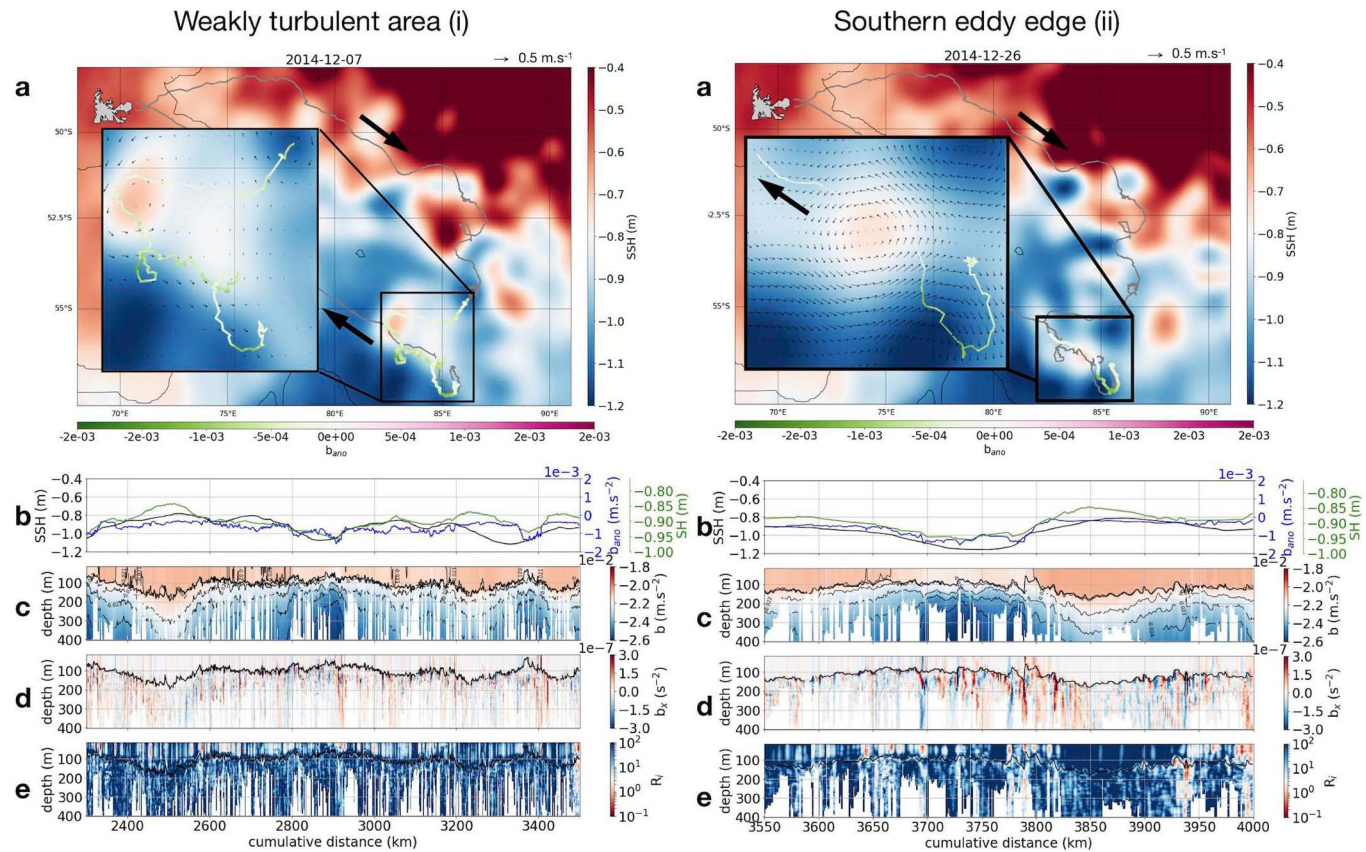
Extended data is available for this paper at <https://doi.org/10.1038/s41561-019-0489-1>.

Supplementary information is available for this paper at <https://doi.org/10.1038/s41561-019-0489-1>.

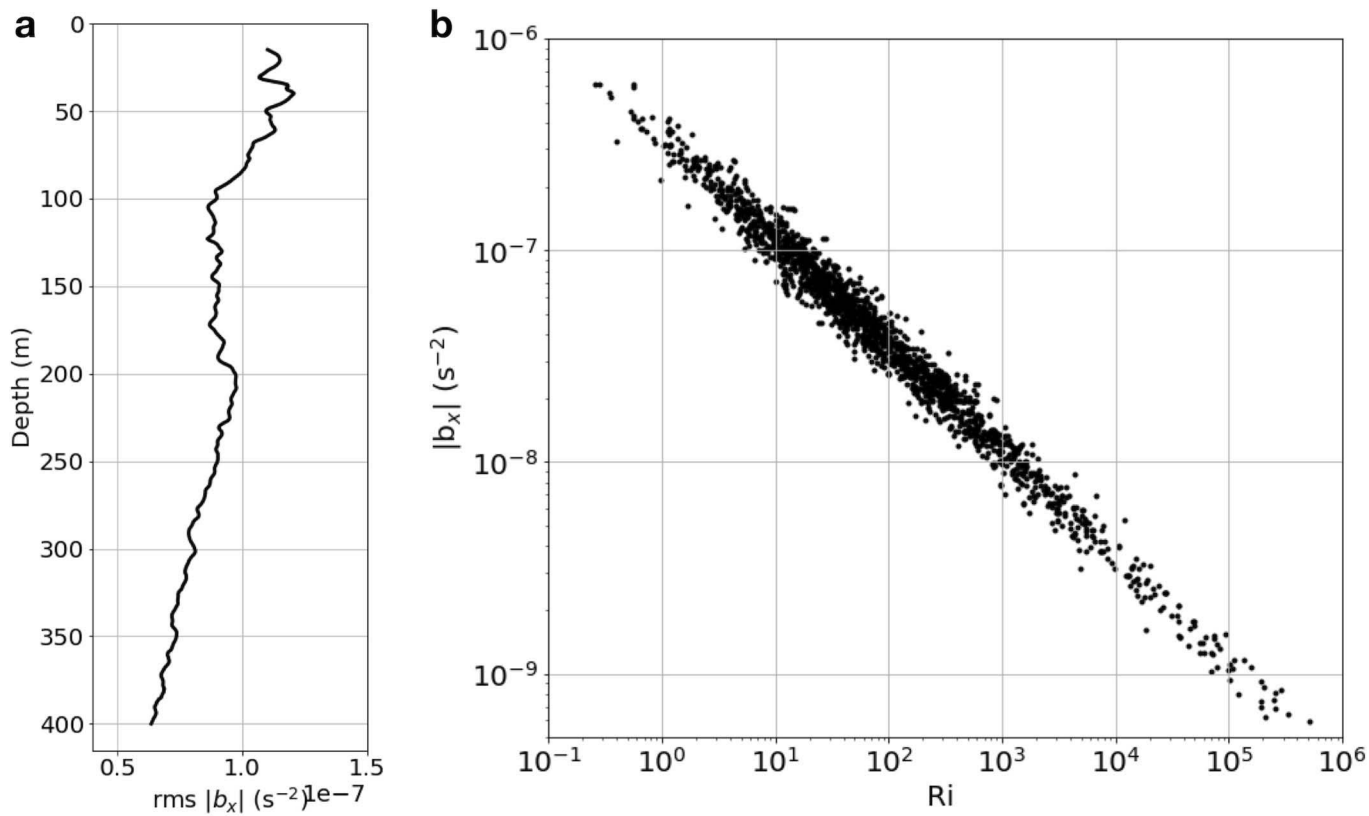
Correspondence and requests for materials should be addressed to L.S.

Peer review information Primary Handling Editor(s): Heike Langenberg.

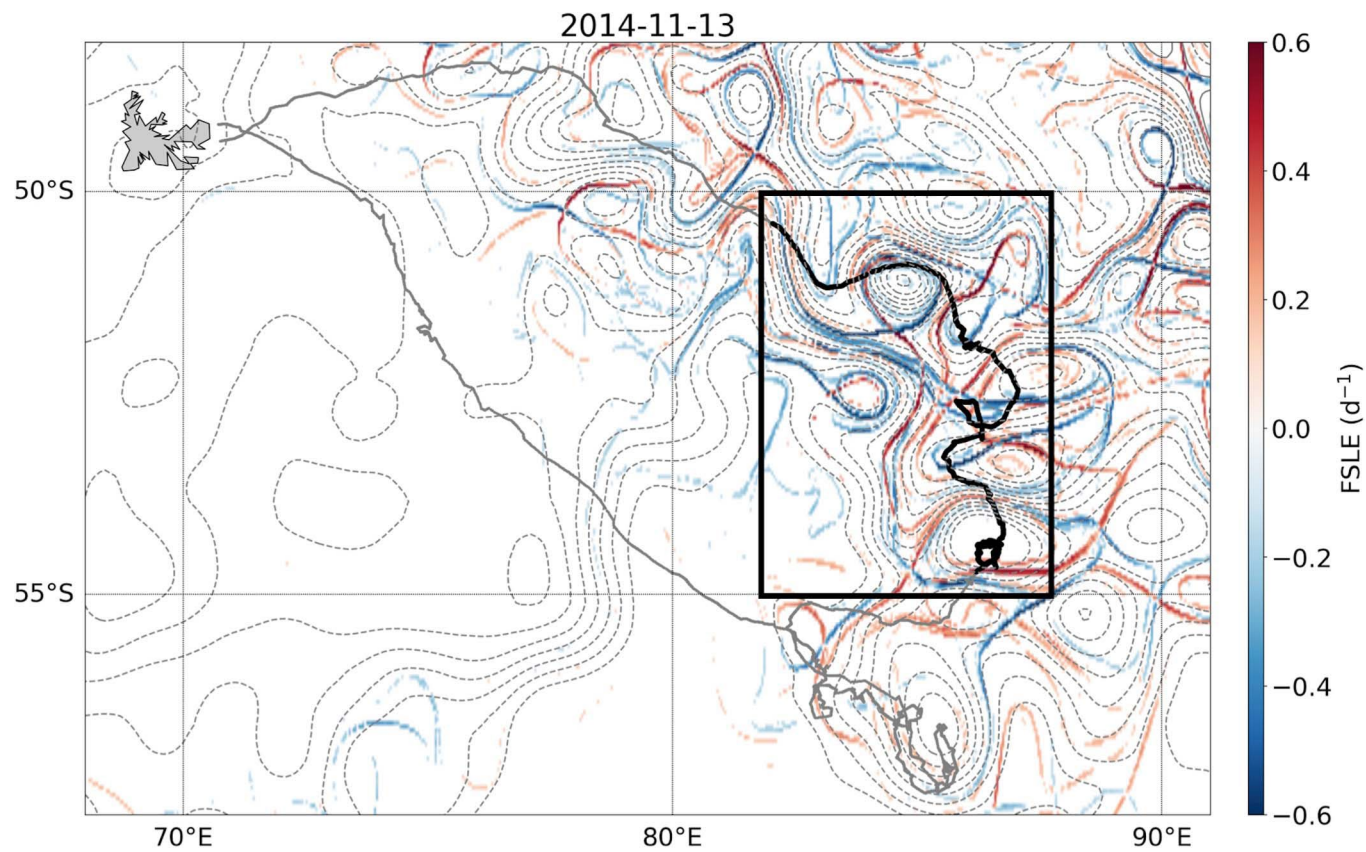
Reprints and permissions information is available at www.nature.com/reprints.



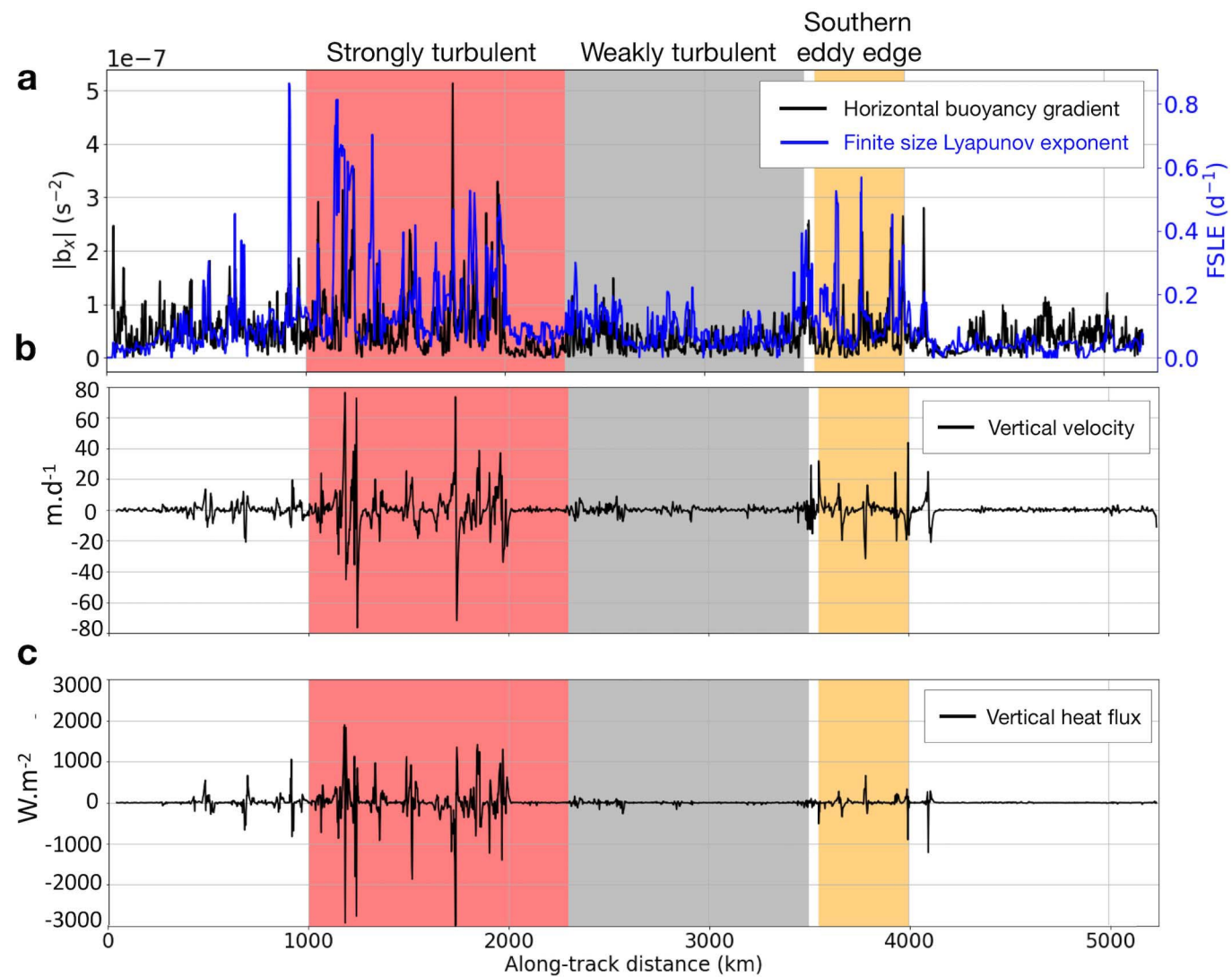
Extended Data Fig. 1 | Weakly turbulent and southern eddy edge areas. Same as Fig. 2 but for i) 2014/11/24 to 2014/12/20 with the SSH snapshot in a) taken on 2014/12/07. The seal crosses a large anti-cyclonic region (grey trajectory in Fig. 1) characterized by weaker currents (smaller SSH anomalies) and referred to as the weakly turbulent area. ii) 2014/12/22-29 with the SSH snapshot in a) taken on 2014/12/26. The seal follows the edges of mesoscale eddies over a distance of ~600 km. This region is referred to as the southern eddy (in orange in Fig. 1). Bold black arrows indicate the direction of the seal.



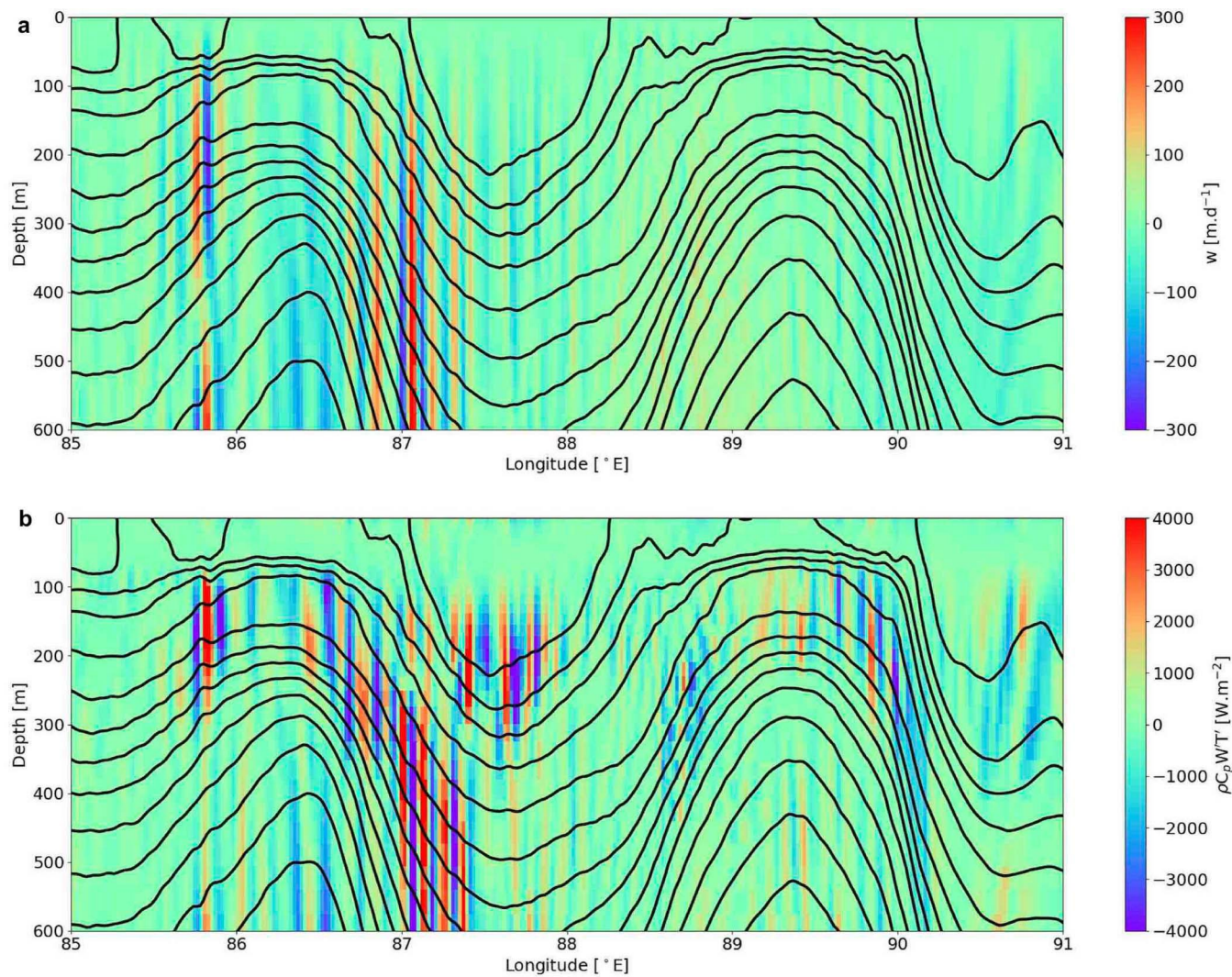
Extended Data Fig. 2 | Lateral gradient of buoyancy and Richardson number in the strongly turbulent area. **a)** RMS of lateral gradients of buoyancy, $|b_x|$, as a function of depth in the strongly turbulent area. **b)** Scatter plot between lateral gradients of buoyancy, $|b_x|$, and Richardson number, Ri , in the strongly turbulent area. $Ri < 2$ coincide with strong buoyancy gradients ($|b_x| > 2.5 \times 10^{-7} s^{-2}$), highlighting the ageostrophic character of the dynamical regime encountered by the seal and the expected strong frontogenesis processes at play.



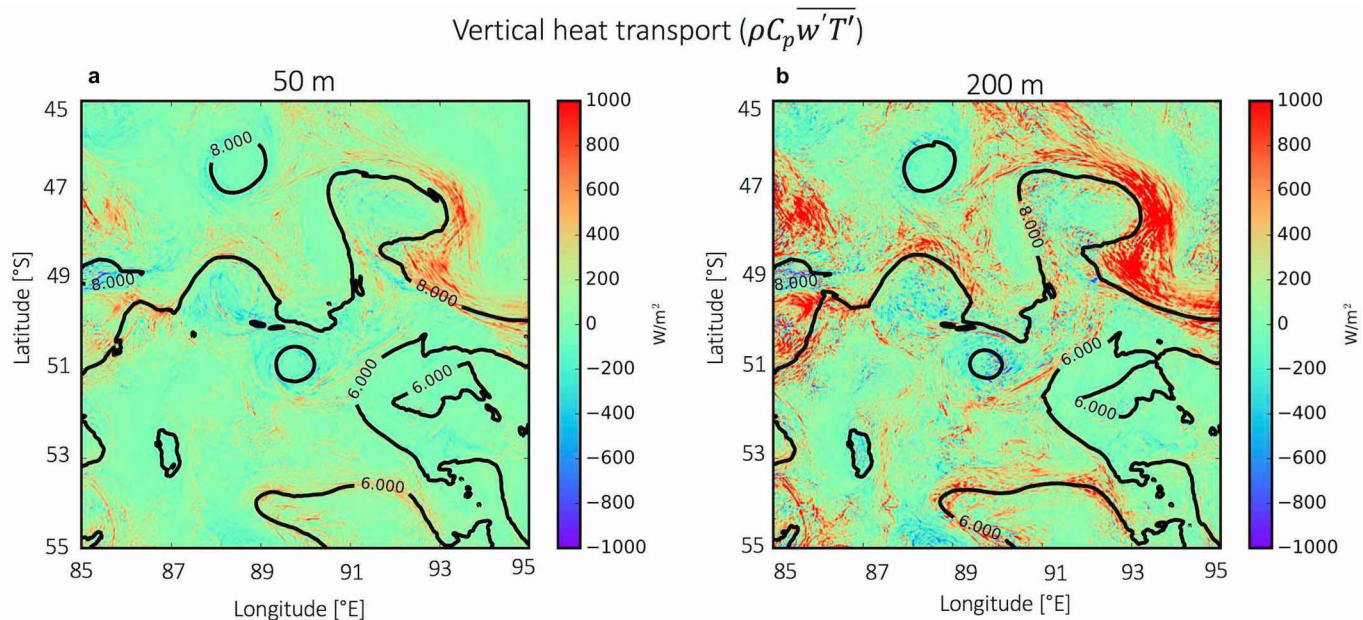
Extended Data Fig. 3 | Map of finite size Lyapunov exponents. Map of FSLE over the entire domain on 13 November 2014. FSLE are greatly enhanced in the strongly turbulent region (black rectangle and in red in Fig. 1) compared to the rest of the domain.



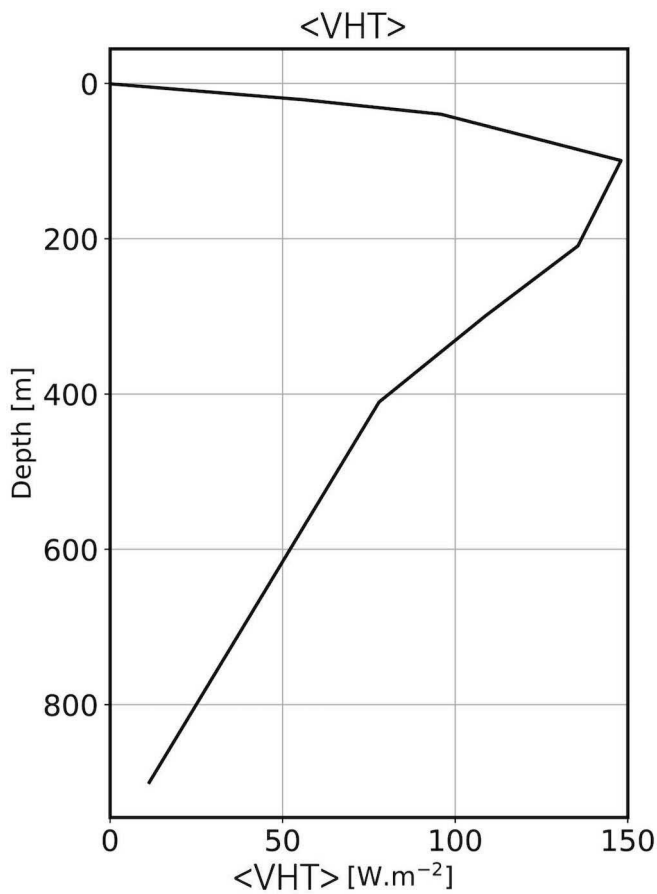
Extended Data Fig. 4 | Finite size Lyapunov exponents and horizontal gradient of buoyancy, vertical velocities and vertical heat transport at 300 m.
 Times series of **a**) Horizontal gradients of buoyancy at 300 m sampled by the seal (in black) and FSLE derived from satellite altimetry along the seal's track (in blue). **b**) Vertical velocities at 300 m derived from the seal and satellite data by solving the omega equation (see main text and Methods). **c**) Vertical heat transport (see Methods). The areas described in the main text and in Fig. 1 are highlighted by the colored rectangles.



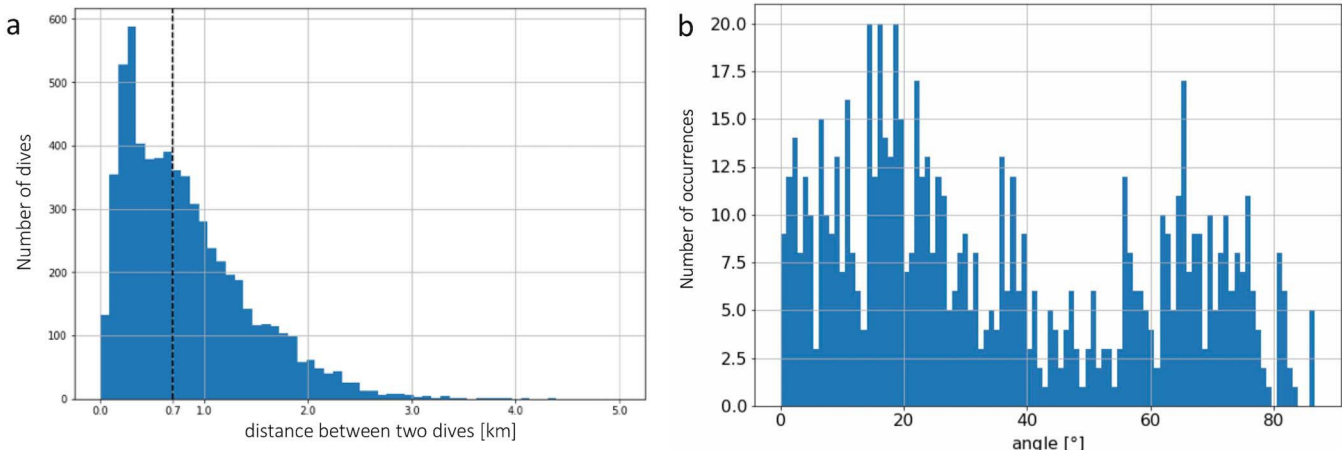
Extended Data Fig. 5 | Daily averaged vertical velocities and vertical heat transport from the high-resolution numerical simulation. Daily averaged vertical section from the high-resolution numerical simulation for November 22, 2011 at 52°S of **a**) Vertical velocities **b**) Vertical heat transport. Isopycnals are shown by the black lines. Enhanced vertical velocities and heat transport with a width of 5–10 km are found in the ocean interior and, in particular, below the mixed layer, similar to the observation presented in the main text.



Extended Data Fig. 6 | Averaged vertical heat transport from the high-resolution numerical simulation. 2-D (x,y) view of 10-day averaged vertical heat transport (VHT) at a) 50 m and b) 200 m. Isotherms are shown in black. Domain averaged values are respectively 92 and 197 W/m². VHT is enhanced at depth and follows the isotherms on the eddy edges, and its averaged value is directed upward (positive value), all of which is consistent with the observational results presented in the main text.



Extended Data Fig. 7 | Domain averaged vertical heat transport from the high-resolution numerical simulation. Monthly averaged vertical heat transport ($\langle VHT \rangle$) as a function of depth over the entire domain from the high-resolution numerical simulation. VHT is directed upwards (positive values) and its magnitude is similar - although even higher - than what is derived from the observational data presented in the main text.



Extended Data Fig. 8 | Distance between two dives and angle between the seal's trajectory and the fronts. **a)** Histogram of the distance between two dives. Median distance between two dives is 700 m (dotted line) and the shortest distance is 100 m. **b)** Histogram of the angle between the seal's trajectory and the stretching FSLE it encounters for $\text{FSLE} > 0.15 \text{ day}^{-1}$. Oblique crossings are most frequent and a normalization is implemented to correct for it (see Methods).